STUDY ON THERMAL-FLOW FIELD CHARACTERISTICS IN MULTI-ANGLE DEICING JET USING PHASE-FIELD AND k-ω TURBULENCE MODELS

Miao GONG [*]***, Huaijin YAN, Hongyi SONG***

Institute of Aviation Engineering, Civil Aviation University of China, Tianjin 300300, China

[*] Corresponding author; E-mail: mgong@cauc.edu.cn

A multi-angle jet model for aircraft deicing under engine-idle conditions was established based on the k-ω turbulence model and introduces the phase-field method to more accurately capture gas-liquid interface behavior. The model's simulation effectiveness was verified through experiments, and the influence of different jet inclination angles (30°, 45°, 60°) on the wall flow field structure, pressure distribution, and heat transfer performance was systematically analyzed based on the simulation results. The research findings indicate that under the condition of a nozzle Reynolds number of 3.2×10^5*, the jet with a 30° inclination angle achieves the optimal comprehensive heat transfer effect on the wall. Its spanwise diffusion range increases by approximately 36 nozzle diameters compared to the 60° case, and the position of the upstream high-temperature core region shifts from x/d = –2.5 to x/d = –13.5. Furthermore, the 30° jet also demonstrates better performance in terms of impact pressure and turbulence intensity. This study provides a theoretical basis for optimizing spray parameters in the engine-idle deicing process and has practical significance for improving deicing efficiency and reducing deicing fluid consumption.*

Key words: *inclined jets; heat transfer analysis; idle deicing; multiphase flow; deicing parameters*

1. Introduction

Aircraft deicing efficiency is a critical factor influencing flight safety and punctuality worldwide [1–3]. To prevent secondary ice accretion on wings and reduce deicing operation time, international airports have implemented engine-idle deicing, which is performed with the aircraft's engines operating at idle conditions [4,5]. This operational approach alters parameters such as the safe working zone of deicing vehicles and the lance height in traditional deicing procedures, which can easily lead to compromised deicing effectiveness and wastage of deicing fluid if mishandled [6–8]. Current research on ground deicing primarily relies on theoretical analysis, with a lack of targeted studies on idle deicing parameters.

In the field of aircraft ground deicing process research, Yakhya et al. [9] pioneered a model for heat transfer in the wall-film region based on RANS methods, proposing that deicing fluid forms a thin liquid film upon wall impingement. Ernez et al. [10] optimized the numerical model by segmenting the deicing process into airborne and near-wall regions, employing a Lagrangian approach for spray particle tracking and an Eulerian method to couple heat exchange between the liquid film and ice layer. Building on this, Ernez et al. [11–12] further refined the model, accounting for fluid miscibility changes during ice melting, and developed a 3D multi-zone model solved via a Lagrangian framework for spray particle equations. Yakhya et al. [13] simulated the initial liquid film formation during deicing onset, investigating multiphase interfaces (liquid PG/water/air) using a Volume-of-Fluid (VOF) model coupled with thin-film dynamics.

Regarding numerical studies of jet impingement, Guo et al. [14] investigated the heat transfer characteristics of impinging jets under varying nozzle geometries and Reynolds numbers (Re), revealing that the Nusselt number (Nu) in the wall-jet region is significantly influenced by radial velocity gradients and jet Re. Zeraatkardevin et al. [15] applied an Eulerian-Lagrangian approach to study jet/spray-wall heat transfer, utilizing the Rosin-Rammler distribution to analyze liquid film thickness, velocity, and heat flux across different wall structures. Hajimohammadi et al. [16] numerically investigated the 3D flow and heat transfer of a turbulent intermittent circular jet impinging on a concave surface using the control volume method and the RNG k-ε model, evaluating the effects of jet Reynolds number and oscillation frequency. Ingole et al. [17] experimentally examined the cooling efficiency of short-range (z/d<10) circular jets (Re<20,000) at inclination angles (θ) of 15°~75°, identifying optimal cooling at θ=45°/60° and correlating Nu with dimensionless θ. Baghel et al. [18] employed the SST-SAS model to study inclined jet cooling, linking changes in near-impingement velocity and turbulence intensity to peak Nu variation. Oliveira et al. [19] reported enhanced stagnation-zone heat flux at small nozzle-to-plate distances (z/d≤10) with increasing Re (9,800~12,000). Hosain et al. [20] analyzed wall-jet heat transfer via boundary layer theory, characterizing the evolution of Nu and film thickness. Liu et al. [21] demonstrated that local film velocity governs liquid film-wall heat transfer during inclined jet impingement, with cooling intensity scaling with impact velocity and temperature differential. Rachdi et al. [22] used the standard k-ω model to analyze the heat transfer characteristics of array nozzles, investigating the coupled effects of plate spacing, jet angle, and nozzle number on heat transfer enhancement. Wang et al. [23] compared dimensionless velocity, turbulent kinetic energy, and wall Nu for different turbulence models and wall functions at z/d=2, finding that the SST and standard k-ω models better simulated turbulence frequency variations in near-wall regions. Yang et al. [24] analyzed short-range impinging jets on concave surfaces based on RANS models and wall treatments, noting that the SST model more accurately predicted the secondary peak in local Nu, though it is primarily applied to high-speed gas flows. Ye Chen [25] analyzed the effects of nozzle-to-plate distance and temperature difference on wall Nu using RANS and LES methods, finding that the v^2f model offered better accuracy at smaller spacings due to its consideration of jet entrainment, while the k-ω model was more accurate for near-wall regions.

This study simplifies the physical model of aircraft engine-idle deicing, focusing on the flow and heat transfer behavior of a thermal jet impinging on a wall surface, thus requiring numerical simulations that accurately capture wall thermal-flow parameters. Based on the current state of jet simulation research, this paper employs the k-ω turbulence model to obtain more precise wall heat transfer parameters. To better simulate the gas-liquid interface behavior and fluid-wall interaction, the phase-field method is introduced and coupled with the k-ω model for solution. Furthermore, current research on inclined jet impingement heat transfer primarily focuses on short-range (z/d<10) cooling of high-temperature surfaces, with limited studies on long-range (z/d>40) impingement heat transfer relevant to idle deicing conditions. Therefore, this study adopts numerical simulation and experimental validation analysis to investigate the flow and heat transfer characteristics of wall jets. Using water as the heat transfer medium at a fixed height of 1 m, jets at inclination angles of 30°, 45°, and 60° are analyzed to examine their flow and thermal performance on the wall. Given that current operational parameters for engine-idle deicing are primarily based on empirical practices and internal manuals at various airports, the data provided by this research can offer valuable support for optimizing idle deicing parameters. This work holds positive significance for improving idle deicing efficiency, reducing deicing fluid consumption, and developing automated intelligent idle deicing stations.

2. Model Develpment and Numerical Simulation

2.1. Principle analysis

The operational process of aircraft engine-idle deicing can be simplified as flow and heat transfer phenomena of an inclined jet impinging on a wall surface. After momentum and energy exchange with the ambient environment in the free jet region, the inclined jet impacts the wall. A high-pressure zone is generated near the impingement point. Upon wall impact, the majority of fluid continues flowing along the jet direction over the wall surface-defined as the downstream region. The zone where fluid flows opposite to the jet direction along the wall from the impingement point constitutes the upstream region, as schematically illustrated in Fig. 1.

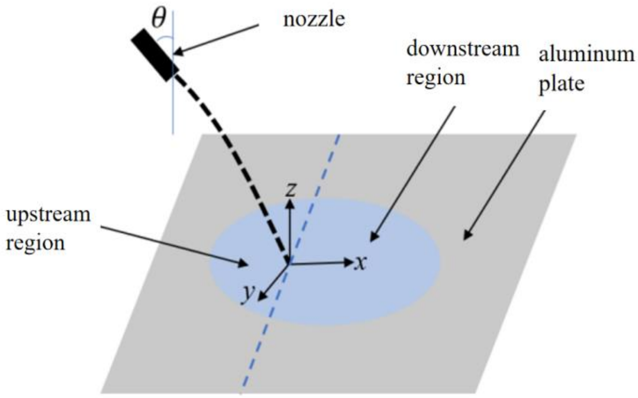

Fig. 1 Schematic diagram of inclined jet

2.2. Numerical Simulation

In studies of nozzle jet fields, the evolution of flow and temperature fields near the wall constitutes the primary research focus. Current numerical approaches for turbulent multiphase flow simulations predominantly include Direct Numerical Simulation (DNS), Reynolds-Averaged Navier-Stokes Equations (RANS), and Large Eddy Simulation (LES). Within RANS methodologies, the k-ω turbulence model is prefered for near wall treatment by many researhers, corroborated by the fact that it is used for the near-wall region in SST model.

Consequently, for analyzing two-phase flow involving immiscible fluids, we adopt a coupled approach integrating the phase-field method with the k-ω turbulence model.

During the solution procedure, the evolution of the binary-fluid interface in the phase-field model is analyzed by incorporating a free energy functional. This enables solving for the volume fraction parameter ϕ within the model, thereby precisely tracking the jet development trends in the phase-field framework. The governing equations are given as follows:

$$\frac{\partial \phi}{\partial t} + \mathbf{u} \cdot \nabla \phi = \nabla \cdot \frac{\gamma \lambda}{\varepsilon_{pf}^2} \nabla \psi \tag{1}$$

where γ denotes the phase-field mobility parameter, λ represents the mixing energy density, and ε_{pf} is the interfacial thickness parameter proportional to the phase boundary width.

During the solution of two-phase flow fields, the phase-field model and k-ω turbulence model achieve mass and energy transfer through the velocity vector field $\mathbf{u}$. Their mutual coupling is governed by the following equations:

$$\rho \frac{\partial \mathbf{u}}{\partial t} + \rho(\mathbf{u} \cdot \nabla)\mathbf{u} = \nabla \cdot \left[-p\mathbf{I} + \mu\left(\nabla \mathbf{u} + \nabla \mathbf{u}^T\right)\right] + F_g + F_{ext} + F_{st} + F \tag{2}$$

where F_g denotes the gravitational force; F denotes the volumetric force; and F_{st} denotes the surface tension force, which governs interfacial evolution within the binary-fluid system.The equations are given as follows:

$$F_{st} = \left(\frac{\lambda}{\varepsilon_{pf}^2}\psi - \frac{\partial f}{\partial \phi} \right)\nabla \phi \tag{3}$$

In turbulence modeling, the transport equation for turbulence kinetic energy k is given by:

$$\frac{\partial}{\partial t}(\rho k) + \frac{\partial}{\partial x_i}(\rho k u_i) = \frac{\partial}{\partial x_j}\left[\Gamma_k \frac{\partial k}{\partial x_j} \right] + G_k - Y_k \tag{4}$$

where P_k represents the turbulence kinetic energy production term due to mean velocity gradients, and Y_k denotes the dissipation rate of k.

The transport equation for the dissipation rate is given by:

$$\frac{\partial}{\partial t}(\rho \omega) + \frac{\partial}{\partial x_i}(\rho \omega u_i) = \frac{\partial}{\partial x_j}\left[\Gamma_\omega \frac{\partial \omega}{\partial x_j} \right] + G_\omega - Y_\omega \tag{5}$$

where P_ω denotes the production term of turbulent frequency due to shear forces, and Y_ω represents the dissipation term of ω.

In the study of heat transfer within two-phase flows, the coupled solution of the phase-field model and k-ω turbulence model resolves the velocity field $\mathbf{u}$, which is subsequently transferred to the solid-fluid heat transfer interface. The influence of temperature T on the two-phase flow solution is addressed through the thermal coupling. For heat transfer analysis in wall jets, the fluid is treated as a weakly compressible medium, with pressure work neglected in the energy equation, yielding the governing heat transfer equation:

$$\rho C_p \frac{\partial T}{\partial t} + \rho C_p \mathbf{u} \cdot \nabla T = \nabla \cdot (k \nabla T) + \tau \cdot \nabla \mathbf{u} + Q_{turb} + Q \tag{6}$$

where C_p denotes the isobaric specific heat capacity of the fluid, k denotes the thermal conductivity, and β denotes the thermal expansion coefficient of the fluid.

2.3. Geometric model and boundary conditions

A small nozzle was selected as the theoretical research object, and its three-dimensional geometry was accurately constructed using UG software, as shown in Fig. 2. To simplify the model, only the internal fluid region of the spray gun was retained, while the remaining structures were replaced with wall boundary conditions, thereby establishing a three-dimensional computational model for thermal-flow field simulation. To ensure that the boundary conditions do not significantly affect the jet flow behavior, the exterior of the computational domain was treated as an infinitely large space, allowing fluid to freely enter and exit. Consequently, all external boundaries of the air domain were set as open boundaries [26]. The edges of the spray gun and the wall boundaries within the computational domain were defined as no-slip wall conditions. Since the de-icing operation under study is unaffected by crosswinds, only one side of the central symmetry plane was modeled to reduce computational load. Additionally, during modeling, the influence of air far from the jet flow path on the velocity and temperature variations of the multiphase inclined jet was considered negligible. Therefore, this portion of the air domain was omitted, and an irregularly shaped air domain adapted to the jet angle was constructed to ensure full development of the jet within the computational domain. Compared to a three-dimensional rectangular computational domain, this modeling approach reduces the number of grid cells by more than two-thirds, while the deviation in computational results is less than 1%. Given the constraints of computational resources and time costs, this domain shape was selected for its economical efficiency. The final computational domain of the model is shown in Fig. 3. Other boundary conditions used in the model are summarized in Table. 1.

Fig. 2 Jet nozzle model

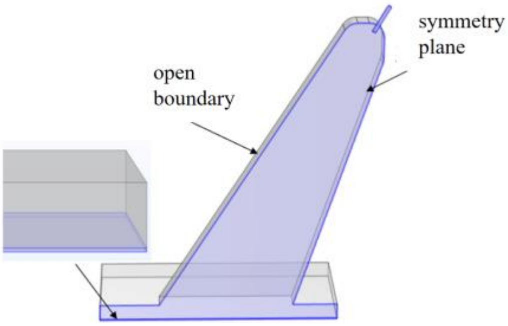

Fig. 3 Calculation domain

Table 1. Parameter settings for model boundary conditions and other parameters

Model Parameters	Set Value
Nozzle Exit Velocity (*u*)	10 m/s
Nozzle Diameter (*d*)	12 mm
Nozzle Height (*z*)	1 m
Aluminum Plate Size	800 mm×800 mm×3 mm
Jet Temperature	353.15 K
Environment Temperature	293.15 K

2.4. Numerical Methods and Solver Settings

The numerical simulations in this study were conducted using the commercial software COMSOL Multiphysics (Version 6.1), which is based on the Finite Element Method (FEM). The governing equations described in Section 2.2, comprising the coupled Phase-Field method, k-ω turbulence model, and energy equation, were discretized and solved within this framework. All numerical models implemented in this work are based on COMSOL's built-in physics interfaces. This study was conducted using the k-ω turbulence model integrated into the Phase Field framework.

In COMSOL, the turbulence flow is solved using the P1+P1 discretization scheme by default. This scheme employs linear shape functions to solve for the fluid velocity and pressure fields. A linear discretization scheme was applied for all other dependent variables. For computing gas-liquid two-phase flow, this approach achieves a balance between computational efficiency and numerical stability.

A segregated solver was employed to solve the coupled system of equations efficiently. The simulations were advanced in time with a fixed time step of 0.1 s over a total physical time of 3 s. The automatic Newton-Raphson method was used as the nonlinear iteration technique, with the convergence criterion for each time step set to a relative tolerance of 0.001. The numerical settings, including the mesh configuration and time-stepping scheme, were validated through a grid independence study (as presented in Section 2.5), ensuring the reliability of the computational results.

2.5. Grid independence verification

In multiphase flow simulations, accurate tracking of the phase interface evolution is essential to ensure computational accuracy. The mesh was constructed using free-form tetrahedral elements. Tetrahedral meshing offers excellent adaptability to complex geometries and can readily handle irregular or intricate models, making it the preferred choice for free meshing strategies. Compared to hexahedral meshing, tetrahedral mesh generation is faster, significantly reducing preprocessing time. When higher accuracy is required, the computational results can be improved by employing higher-order elements. The mesh was refined in the main airborne region of the jet to achieve more accurate volume fraction results, while the nozzle and impingement wall region was also refined and enhanced with boundary layer elements. To ensure that the mesh settings did not affect the computational results, a comparison was conducted using different mesh sizes. The mesh quality was evaluated using the standard skewness criterion, and all meshes achieved a skewness value above 0.69, ensuring the accuracy of the fluid flow and heat transfer calculations [27]. The mesh distribution is shown in Fig. 4.

When the mesh density reached a certain level, the thermal-flow field results became independent of the meshing method, indicating convergence of the solution. Taking the case with a jet inclination angle of 30° as an example, the velocity profiles along the central axis of the wall for geometric models with different mesh sizes are shown in Fig. 5 (wallcenterline velocity at t=0.5 s, θ=30°), with errors within 5%. The same mesh generation strategy was applied to models with different jet inclination angles, and the resulting mesh details are summarized in Table.2.

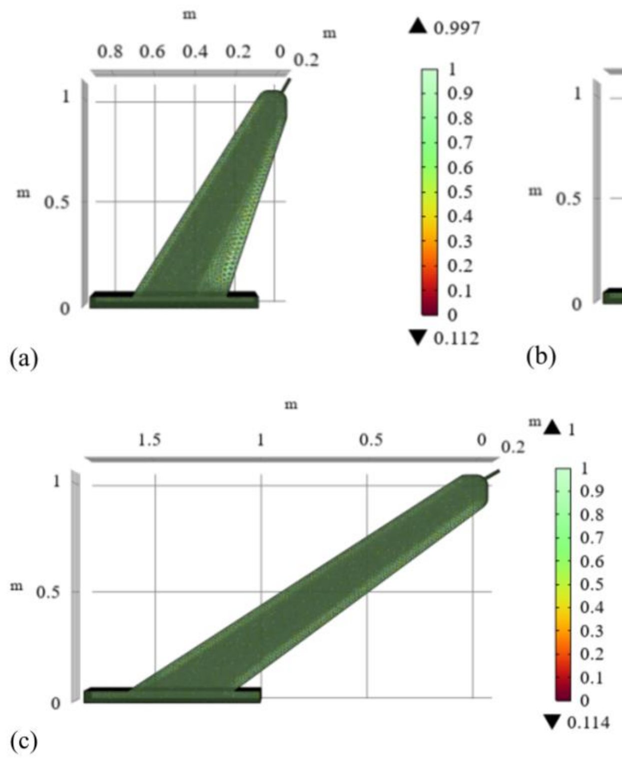

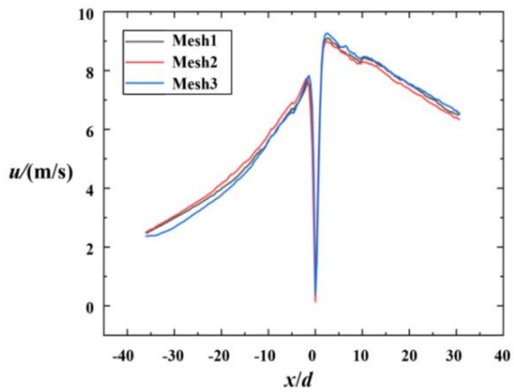

Fig. 4 The mesh distribution; (a)θ=60°, (b)θ=45°, (c)θ=30°

Fig. 5 Verification of grid independence

Table 2. Number of grids for different jet inclination conditions

Jet Inclination Angles (θ) /°	Number of Mesh / million		
30°	1.55	1.73	1.90
45°	1.48	1.74	1.98
60°	1.99	2.26	2.51

3. Experimental Validation of Inclined Jet Flow Fields

3.1. Experimental equipment and experimental plan

To ensure the accuracy of the adopted model, a small-scale experimental platform for inclined jet impingement was constructed. Focusing on a simplified de-icing jet under the model's operating conditions, experiments were conducted in an ambient-temperature environment. The experimental system consists of a pressurization pump, flow regulating valve, flow meter, and measurement instrumentation, with the schematic diagram illustrated in Fig. 6.

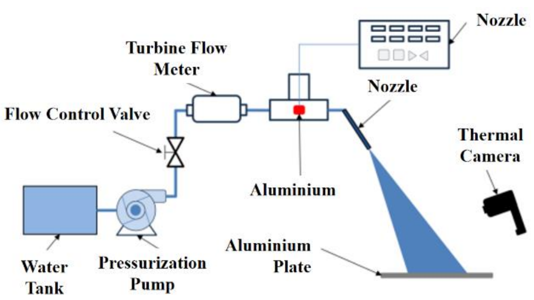

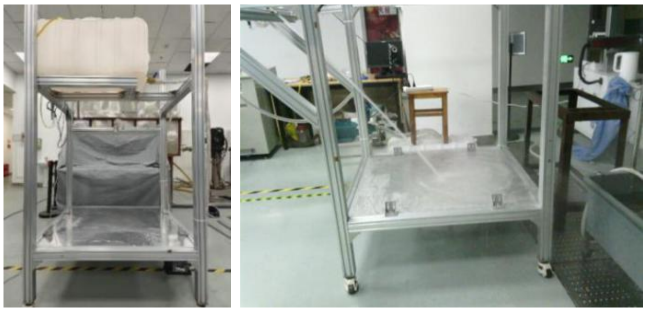

Fig. 6 Experimental schematic diagram **Fig. 7 The Experimental platform**

The experimental platform was constructed using 6060 aluminum profiles, with a 1m×1m×3mm aluminum plate serving as the base surface. During experiments, parameters such as jet height and inclination angle were adjusted by repositioning the aluminum profiles connected to the nozzle. Fluid from the reservoir was first drawn by the pressurization pump, with main pipeline flow regulated by the flow control valve and measured by the flow meter. A PT100 thermal resistance sensor measured fluid temperature at the outlet (measurement range: 0~100℃). The aluminum plate functioned as the impingement surface, with temperature data captured using a handheld thermal camera[28].

During experimentation, fluid temperature progressively decreased as it was drawn from the reservoir through the pressurization pump. Consequently, repeated preliminary tests were conducted at the initial stage, with subsequent tests maintained at 80°C outlet temperature regulated by the PT100 sensor. Prior to formal testing, preliminary experiments were performed to calibrate thermal camera parameters including emissivity settings. In these preliminary jet tests, PT100 sensors were mounted at designated locations on the aluminum plate while a four-channel temperature monitor simultaneously logged fluid temperatures at four positions. Thermal camera parameters were calibrated by comparing thermocouple readings with thermal mapping results to prevent measurement distortion due to improper configuration.

3.2. Experimental uncertainty analysis

(1) During the experiment, due to a certain delay in the thermal imager, there is a discrepancy between the time points captured by the thermal imager and the fixed time points in the simulation process; (2) When using a thermal imager for data collection, capturing images from the side of the experimental system may cause temperature distortion in areas far from the shooting point due to the pixel limitations of the thermal imager; (3) Due to the high reflectivity of the aluminum profile, there is a certain error in temperature measurement in the edge areas of the wall far from the impact point.

3.3. Comparison of experimental results and simulation data

For varying inclination angles, the numerical simulations and experimental results demonstrate generally consistent trends. The *k-ω* turbulence model provides satisfactory predictions in the downstream region of inclined jets, with optimal agreement between simulation and experiment observed at 30° inclination. As shown in Fig. 8.

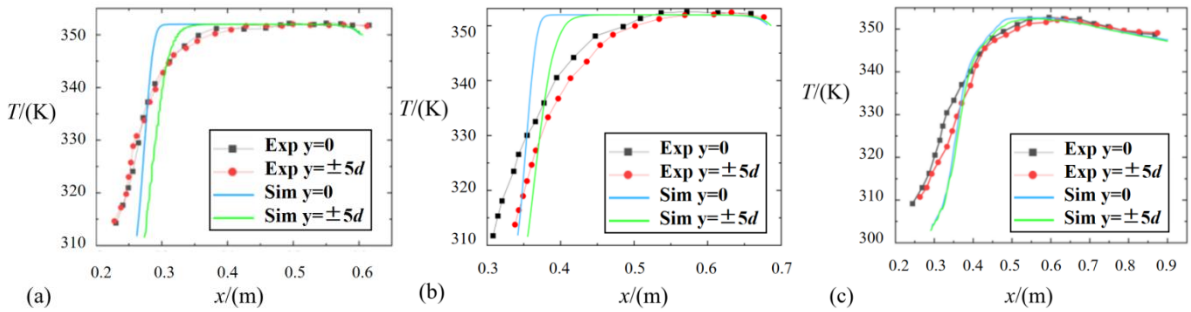

Fig. 8 Comparison of experimental and simulation results at different locations on the wall surface; (a)θ=60°, (b)θ=45°, (c)θ=30°

Significant discrepancies between numerical simulations and experimental data are observed in the upstream wall region, with particularly pronounced errors at 45° and 60° inclination angles. This deviation may originate from the coupled solution process of the phase-field model and *k-ω* turbulence model at the phase interface. During this process, a distinct two-phase interface forms in the far upstream region, inducing an artificially rapid temperature decline in the simulated upstream zone at 45° and 60° inclinations. This computational artifact contributes substantially to the observed simulation errors. During experimental measurements, thermal latency inherent in the infrared thermography system introduced temporal misalignment between captured data points and fixed simulation time steps. Concurrently, pixel resolution limitations of the thermal camera generated measurement uncertainty in temperature readings within the far upstream region near the impingement point.

Compared to the downstream wall region, the relatively thin thermal boundary layer in the upstream impingement zone leads to potential underprediction of thermal diffusivity by the *k-ω* turbulence model. This results in underestimated heat transfer capabilities within this region. When the impinging jet generates adverse pressure gradient-induced reverse flow in the upstream area, complex local flow structures emerge, characterized by significant vortical structures and secondary flow patterns. The computational accuracy of turbulent kinetic energy distribution along the upstream wall is compromised by the *k-ω* model's treatment of turbulence dissipation rate, consequently distorting predicted temperature profiles. Furthermore, at higher inclination angles, diminished streamwise momentum near the upstream impingement zone enhances flow susceptibility to ambient disturbances.

This amplifies temperature gradient inaccuracies in far-upstream simulations, ultimately generating substantial simulation discrepancies.

In the downstream wall region, numerical simulations demonstrate close agreement with experimental data, with the model accurately capturing high-heat-flux zones. For turbulence-dominated heat transfer processes along the wall surface, the coupled k-ω turbulence and multiphase model effectively resolves fluid thermal transport characteristics in these high-heat-transfer regions through precise tracking of turbulent features and thermal exchange dynamics. While minor discrepancies persist in areas remote from the stagnation point, this methodology reliably predicts fluid thermal evolution patterns within acceptable tolerances.

4. Analysis of Simulation Result

To systematically investigate the evolution of wall thermal-flow fields under varying jet inclination angles, this study conducts simulations at a fixed Reynolds number of Re = 3.2×10^5. The heat transfer characteristics and flow dynamics are analyzed for inclination angles of 30°, 45°, and 60°, with emphasis on near-wall thermal boundary layer development and stagnation zone phenomena.

4.1. Analysis of Wall-Jet Pressure Characteristics

When a high-temperature, high-velocity fluid impinges on a wall, its kinetic energy is converted into pressure. As the jet inclination angle changes, the stagnation point of the jet impact shifts. Plot the pressure distribution along the wall centerline for different jet inclination angles based on the data, as shown in Fig. 9. For all inclination angles, the high-pressure zone on the wall resides within $\pm 5d$ from the pressure peak. This region exhibits the highest pressure across the entire wall surface. Pressure decreases rapidly as the jet diffuses away from the impingement point. The maximum pressures for jet inclination angles of 45° and 30° were 2.97×10^5 Pa and 2.93×10^5 Pa, respectively. At θ = 60°, the peak pressure was 1.98×10^5 Pa, representing a decrease of approximately 33%. In practical deicing operations, the impingement pressure helps clear snow and ice from the aircraft surface. This is particularly effective for loose, low-viscosity snow types, where direct removal is more efficient. Therefore, when the jet inclination angles are 45° and 30°, the wall experiences greater impact force, resulting in better snow removal capability under non-thermal conditions (i.e., without involving heat transfer for melting).

Fig. 10 presents the wall pressure distribution for different jet inclination angles. The spatial extent of the high-pressure region on the wall shows minor variation across inclination angles. At 60° inclination, the high-pressure zone exhibits an elliptical distribution extending towards the downstream region of the wall. Here, the jet exerts a stronger transverse impact force on the downstream region. At this angle, ice removal primarily relies on the impact force detaching the ice layer from the wall surface. In contrast, inclination angles of 30° and 45° produce a more uniform circular high-pressure distribution. For the 45° jet, wall pressure exceeds 95% of the peak value within an elliptical region defined by $-1.14 < x/d < 1.14$ and $-1.20 < y/d < 1.97$. At 60° inclination, this elliptical high-pressure zone ($p > 0.95 p_{max}$) contracts to $-1.67 < x/d < 1.33$ and $-1.15 < y/d < 1.15$, representing an approximately 5% reduction in area.

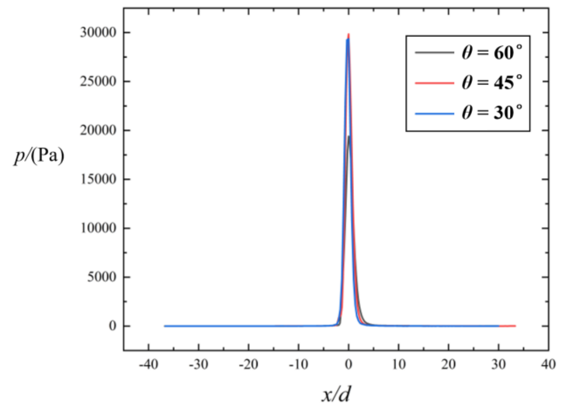

Fig. 9 Plot of *x*-axis upward pressure on the wall for different jet inclinations

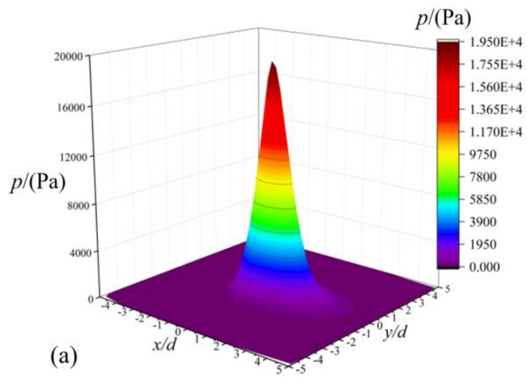

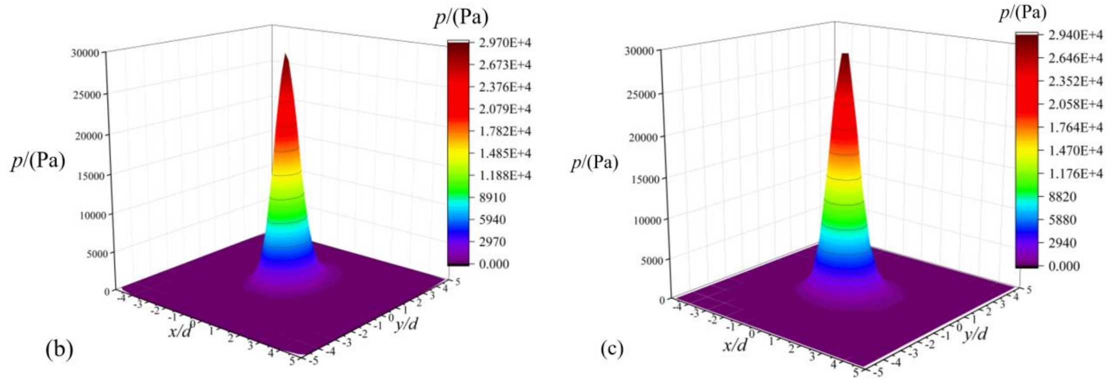

Fig. 10 Pressure map of the region near the impact point for the different jet inclination angle; (a)θ=60°, (b)θ=45°, (c)θ=30°

4.2. Jet Velocity Field Analysis

4.2.1 Velocity Profile of Free Jet

To investigate the velocity and temperature distributions of inclined jets on wall surfaces, understanding the development characteristics of inclined jets in air is essential. As shown in Fig.11, when t<0.2 s, the inclined jet rapidly develops along the nozzle direction under gravity while maintaining its primary trajectory. For inclined jets, convective mixing with ambient air causes radial expansion in the free jet region. Under all three inclination angles, the fluid reaches the wall at t=0.3 s.

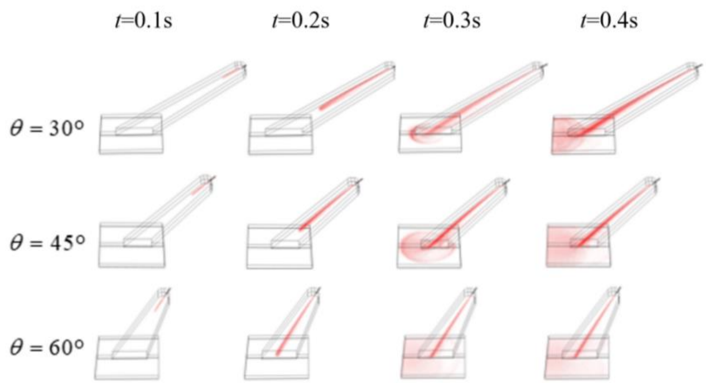

Fig. 11 Schematic diagram of volume fraction in impinging jet

According to the modified Richardson number (Ri)[29]:

$$Ri = \frac{g\,sin\,\theta \cdot \left(\rho_a - \rho_{jet}\right)}{\rho_{avg} \cdot \left(\dfrac{\partial U_z}{\partial y}\right)^2} \tag{7}$$

where ρ_α is the ambient density, ρ_{jet} is the jet density, and ρ_{avg} is the average density.

Based on calculations, the Richardson number (Ri) is less than 0.25 under all three inclination angles. After the fluid is ejected from the nozzle, the main jet is dominated by inertial forces and exhibits strong instability near the nozzle. As the inclination angle increases, the horizontal momentum of the jet increases, and the transverse velocity gradient in the shear layer intensifies, making the flow more susceptible to Kelvin-Helmholtz (K-H) instability.

Under different jet inclination angles, the velocity and jet height were non-dimensionalized to obtain Fig. 12. When the jet enters the air from the nozzle, it flows from a high-pressure region to a low-pressure region, converting pressure energy into kinetic energy, which results in an increase in jet velocity within this region. At jet inclination angles of 30°, 45°, and 60°, the maximum values occur at z/d = 1.69, 1.48, and 2.14, respectively. As the jet develops, a high velocity gradient exists between the jet and the surrounding air. Due to instability in the interfacial boundary layer, energy and momentum are transferred in the form of turbulent vortices through shear interaction with the ambient air in the free jet region near the nozzle, leading to significant energy dissipation in the main jet. At $z/d \approx$ 6.51, 6.67, and 6.92, the velocity of the main jet equals the exit velocity.

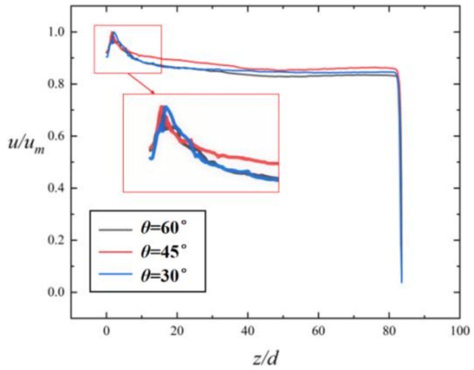

Fig. 12 Velocity variation in air for different jet inclinations

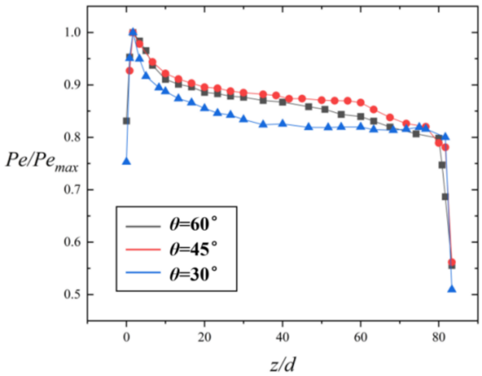

Fig. 13 Pe diagram of jet in the air

Regarding thermal dissipation in airborne jets, the Péclet number (Pe) characterizes the relative dominance of convective heat transfer to thermal diffusion within the jet bulk. Its expression is given by:

$$\mathrm{Pe} = \frac{Lu}{\alpha} = \frac{Lu}{k/(\rho Cp)} \tag{7}$$

where L denotes characteristic length (e.g., nozzle diameter), u denotes local flow velocity and α denotes thermal diffusivity. Fig. 13 presents the normalized Péclet number distribution for the free jet, depicted as a line plot with data points.

For the stabilized jet flow field, analysis was conducted combining the dimensionless Péclet number (Pe) and the temperature drop in the central region of the airborne jet (Fig. 14). Within the range of $0 < z/d < 5.01$, the temperature in the core region of the inclined jet decreases relatively rapidly. In this interval, enhanced turbulent effects in the main jet lead to continuously improving convective heat transfer capacity.

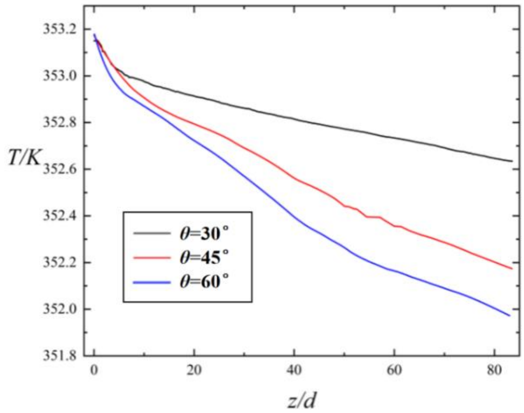

Fig. 14 Temperature of water jet in the central area of the air

Although the jet is not fully broken up in this region, Kelvin–Helmholtz (K–H) instability generates vortices in the shear layer, which intensify heat exchange between the boundary layer and the ambient environment.

At a jet inclination angle of 30°, the temperature decreases by approximately 0.13 K in this interval. For jet inclination angles of 45° and 60°, the corresponding intervals are $0 < z/d < 4.86$ and $0 < z/d < 3.63$, respectively. Within these ranges, the temperature drop in the main jet is about 0.15 K and 0.18 K, respectively. Results show distinct characteristics across jet inclination angles in Table. 3. Larger jet inclination angles yield progressively lower bulk temperatures at identical elevations. During jet development within $5.01 < z/d < 80$, convective flow attenuation reduces turbulence intensity, causing the Péclet number to decline. Consequently, the convective heat transfer capacity of the jet bulk diminishes with increasing downstream distance.

Table 3. The thermal core region and temperature reduction

Jet Inclination Angles (*θ*) /°	The Thermal Core Region(*z*/*d*)	Temperature Reduction / K
30	$0 < z/d < 5.01$	0.13 K
45	$0 < z/d < 4.86$	0.15 K
60	$0 < z/d < 3.63$	0.18 K

4.2.2 Wall Flow Field Distribution

Fig.15 displays the near-wall velocity distribution under different jet inclination angles at $t = 3$ s. As observed, the fluid velocity reaches its maximum near the stagnation point following wall impingement across all inclination conditions. Compared to other angles, $\theta = 30°$ yields the highest peak wall velocity of 9.26 m/s.

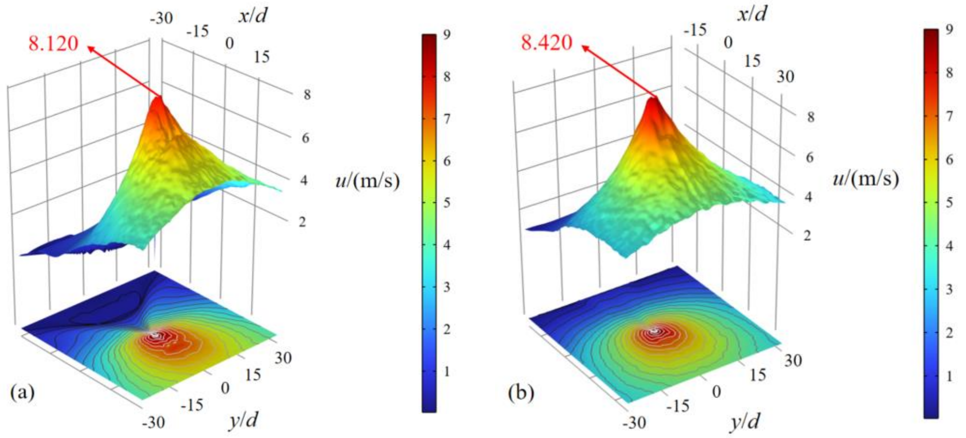

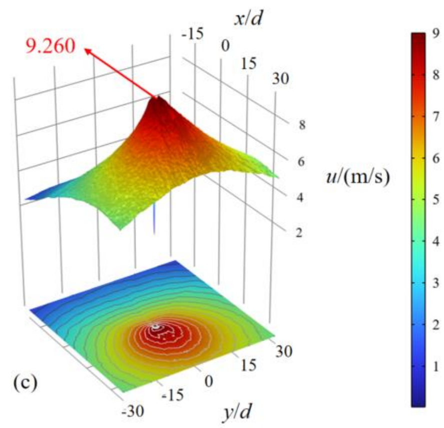

Fig. 15 Wall velocity diagram for different jet inclination conditions; (a)θ=60°, (b)θ=45°, (c)θ=30°

For jets at varying inclination angles, velocity distributions within high-pressure wall regions follow identical trends. Relative to the wall stagnation point (origin), velocity increases rapidly with radius when r/d<1. Within 1<r/d<5, wall velocity decreases with radial distance. Significant velocity gradients occur across inclination angles in this region: 30° jets exhibit 6.89~9.26 m/s, 45° jets show 5.87~8.38 m/s, and 60° jets demonstrate 6.46~8.07 m/s. In the downstream region (x/d>0, y/d>0), velocity decreases with increasing x/d and y/d. At 30° inclination, high-velocity zones concentrate within 20d of the stagnation point, where elevated flow velocities significantly enhance convective heat transfer.

The 60° jet exhibits distinct momentum transfer characteristics: primary momentum aligns with the +x-direction, concentrating high-speed zones more sharply in the downstream region with pronounced elliptical distribution. Consequently, upstream slope velocities drop below 3.5 m/s at r/d>15. Higher inclination angles progressively concentrate velocity toward the +x-direction. This accelerates velocity decay along the y-direction, impairing convective heat transfer at high y-locations in the downstream region.

For the wall jet Reynolds number, the characteristic length is taken as the nozzle diameter d (consistent with the jet orifice definition). The calculation formula is given by:

$$\mathrm{Re} = \frac{\rho u d}{\mu} \tag{8}$$

Under inclined jet conditions, changes in inclination angle directly alter near-wall flow behavior. Under all three inclination angles, the wall jet region downstream of impingement sustains elevated Reynolds numbers (Re) with fully turbulent flow. Fig.16 presents the corresponding near-wall Re distributions for each inclination configuration. At identical nozzle Reynolds numbers, increased inclination amplifies in-flight momentum losses. Upon wall impact, momentum converts to static pressure within ±2.5d of the stagnation point, creating maximum static pressure and minimum Re at the impingement zone. Maximum Re occurs in the downstream region, with values of 2.64×10^5, 2.74×10^5, and 2.91×10^5 for 30°, 45°, and 60° inclinations respectively. Compared to 60°, maximum Re increases by approximately 4.5% at 45° and 13.3% at 30°. Higher inclination angles enhance the radial velocity component parallel to the wall before impact. Consequently, fluid flux toward the upstream region diminishes. The high-Re zone on the upstream region contracts by 2.4*d* at 45° and 4.1*d* at 60° relative to 30°. This results in substantially lower Re values in distal upstream regions at 60° inclination, where flow approaches laminar conditions.

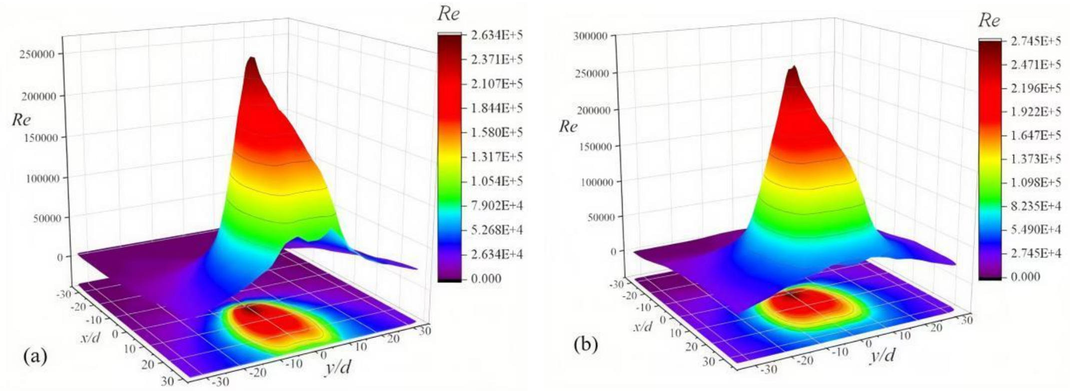

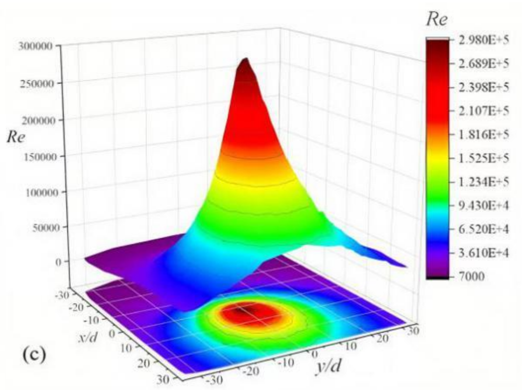

Fig. 16 Re diagram of the wall for different jet inclinations; (a)θ=60°, (b)θ=45°, (c)θ=30°

Analysis of Reynolds number distributions reveals that inclination angle affects wall heat transfer primarily by altering flow regimes. Defining the high-Re zone boundary at $Re=10^5$, Table. 4 delineates elliptical boundaries of these regions across inclination angles. The high-Re zones exhibit elliptical distributions on the wall under all tested conditions. At 30° inclination, the high-Re zone covers the largest area, while 45° and 60° configurations reduce this area by approximately 30.6% and 36.5%, respectively. Increasing inclination progressively suppresses spanwise spreading of high-Re zones in the downstream region. This transforms the near-circular distribution at 30° into increasingly flattened configurations. Compared to 30° inclination, 45° and 60° reduces maximum spanwise spread by approximately 5.2*d* and 9.12*d*, respectively. Conversely, streamwise spreading in the downstream region increases with inclination. Relative to 45°, 30° and 60° extends streamwise spread by approximately 3.1*d* and 4.1*d*, respectively.

Table 4. High re region under different tilt angle conditions

	θ=30°	θ=45°	θ=60°
x_1/d	28.21	25.10	29.26
x_2/d	–6.17	–3.75	–2.04
y/d	±16.15	±13.35	±11.59

For jets inclined at 60° and 45°, a low-Re zone was observed within the streamwise location range $8 < x/d < 9$. The Re value in this zone was approximately 73% to 76% of the peak Re value. This reduction is attributed to the occurrence of hydraulic jump following the initial jet impingement on the wall. Following secondary impingement of the fluid on the wall, a secondary Re peak emerged in the downstream region of the wall. The magnitude of this secondary peak was approximately 80% of the maximum wall Re. As the jet spreads further downstream, the wall Re continuously decreases.

4.2.3 Velocity distribution along the centerline in the spanwise direction of the wall surface for jets at different inclination angles

For inclined jets, after impinging on the wall, the fluid volume is diverted downward along the slope from the impingement point. This results in the concentration of fluid velocity and momentum transfer predominantly in the downstream region, consequently affecting the heat transfer in the upstream region of the wall. As the jet inclination angle increases, the velocity asymmetry between the upward and downstream regions on the wall becomes more pronounced. Fig. 17 illustrates the variation of spanwise fluid velocity on the wall surface normal to the jet centerline axis at different jet inclination angles. It can be observed that the spanwise velocity distribution of the wall jet exhibits a distinct "secondary bimodal peaks" phenomenon. Following wall impingement, momentum redistribution leads to a symmetric velocity profile near the impingement point.

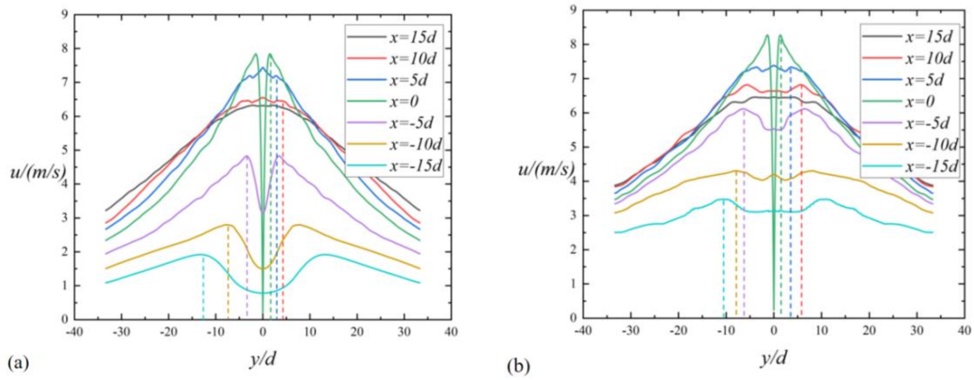

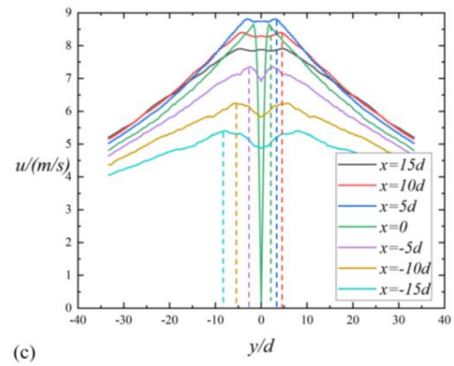

Fig. 17 Spreading velocity distribution on the wall with different jet inclinations of *t*=3 s; (a)*θ*=60°, (b)*θ*=45°, (c)*θ*=30°

In the downstream region of the wall ($x > 0$), the wall-jet velocity is higher, with the peak velocity occurring at a smaller spanwise distance from the stagnation point. As x increases, the fluid continuously diffuses along the wall with progressive velocity decay and reduction in peak magnitude. At 60° jet inclination, along the x/d=0 axis, the velocity reaches its maximum (7.85 m/s) near y/d=±1.5. The velocity along the x/d=0 line decays most rapidly in the y-direction. At y/d=±33.3, the velocity is 2.34 m/s. As the selected x-position moves away from the wall stagnation point, the velocity profile gradually smooths, and the spanwise location of the peak velocity shifts farther from y=0. This indicates progressively gentler velocity variations in the downstream region with increasing distance from the stagnation point.Compared to the downstream region, velocities in the upstream region are significantly lower. At x/d= –5, the maximum velocity (4.82 m/s) occurs at y/d=±3.36. Velocity attenuation becomes more pronounced with further displacement from the stagnation point. At x/d= –15, the peak velocity (1.92 m/s) appears at y/d=±13. When x/d< –10, wall velocities remain below 2.79 m/s. The heightened velocity asymmetry between slope regions at 60° inclination causes significantly degraded heat transfer performance in the upward-slope zone compared to other inclination angles.

At 45° inclination, fluid momentum concentrates predominantly in the downstream region. Velocities exceed 3.08 m/s for $x/d > -10$. The upstream region exhibits notably enhanced velocities, resulting in improved heat transfer intensity. For 30° inclination, wall velocities consistently exceed 4.06 m/s except within the stagnation zone. The global maximum velocity (8.90 m/s) occurs at x=0, y/d=±1.73. Higher fluid velocities promote more significant spanwise diffusion along the wall, yielding a more uniform distribution and expanded heat transfer coverage. Even in the far upstream region (x/d= –15), the local velocity maximum (5.39 m/s) occurs near y/d=±7.79. Core-region velocities are comparatively higher than at other inclinations.

Across all inclination angles, high-velocity zones primarily concentrate within $-10<y/d<10$. At 30° inclination, fluid velocities in this region exceed 7 m/s, while velocities approximate 6 m/s at 60° inclination.This results from greater aerodynamic losses during free-jet development at steeper angles—where larger nozzle-to-wall horizontal distances under equivalent jet heights reduce impingement energy.

4.3. Wall Surface Temperature Field Analysis

4.3.1 Wall Surface Temperature Distribution

Fig.18 displays wall surface temperature contour plots (with colorbars) at the same instant (t=3 s) for different jet inclination angles. It can be observed that under all three inclination conditions, the central wall region reaches the maximum temperature (352 K), with high-temperature zones predominantly concentrated in the downstream region.

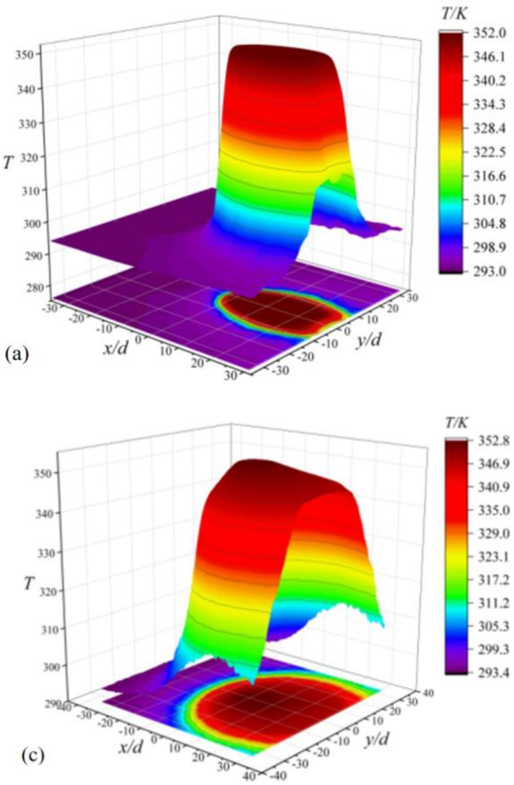

Fig. 18 Plot of wall temperature at different jet inclinations; (a)θ=60°, (b)θ=45°, (c)θ=30°

At 30° jet inclination, high-temperature zones primarily concentrate within $0<x/d<20$ and $-15<y/d<15$, with the central thermal core exhibiting circular radial diffusion. Temperatures remain elevated (346.9 K) in the region bounded by $x/d > -8$ and $-19.2<y/d<19.2$. Along the aluminum plate edge in the downstream region, wall-adjacent fluid temperatures consistently exceed 317.2 K. Along the jet-aligned edge of the aluminum plate, temperatures consistently exceed 333.54 K within the range of $-20 < y/d < 20$. Significant thermal gradients develop with increasing distance from the impingement point. In the upstream region along y/d=0, temperature decreases to 320.4 K at x/d= –10. Equivalent temperature positions: x/d=–4.71 at 45°; x/d=–3.24 at 60°. The 30° case exhibits approximately 6~7d greater thermal influence extent along y/d=0 in the upstream region compared to other inclination angles. At 45° jet inclination, along the x/d=0 axis, temperature decays radially from the jet center reaching 310 K approximately at y/d=±10. Within the region bounded by $-10<y/d<10$ and $-5<x/d<22.9$, fluid temperatures consistently exceed 342.2 K. Compared to the 30° case, both 45° and 60° inclinations exhibit more concentrated high-temperature zones. This concentration occurs because steeper inclination angles enhance inertial-driven flow toward the downstream region post-impingement, retarding spanwise diffusion and producing distinct elliptical temperature distributions.

Using 333.15 K (60°C) as the thermal boundary threshold, at 45° jet inclination the maximum spanwise diffusion occurs at (x/d=10.6, y/d=±13.0). Under this criterion, the spanwise boundary coordinates of the jet expansion on the wall surface are defined by (x/d=12.2, y/d=±7.8) at 60° and defined by (x/d=13.3, y/d=±25.8) at 30°.Compared to 30° and 45° inclinations, the 60° jet exhibits approximately 10d and 36d reduction in spanwise extension of high-temperature fluid within the downstream region, respectively.

4.3.2 Wall Surface Nu Distribution

For thermal energy transport processes on wall surfaces, the Nusselt number (Nu) is conventionally employed to quantify the intensity of convective heat transfer, defined as follows:

$$\mathrm{Nu} = \frac{hD}{k} \tag{9}$$

where h denotes convective heat transfer coefficient [W/(m²·K)], d denotes nozzle diameter (characteristic length), k denotes thermal conductivity of the fluid [W/(m·K)].

The Prandtl number (Pr), a dimensionless parameter dependent on material properties, is calculated as:

$$\mathrm{Pr} = \frac{\nu}{\alpha} = \frac{\mu Cp}{k} \tag{10}$$

For convective heat transfer during inclined jet impingement, the high-velocity fluid enhances heat transfer upon wall impact. Consequently, Nu > 1 prevails across the wall surface except within the stagnation zone, as shown in Fig.19. For high-temperature water jets, elevated temperatures reduce viscosity, decreasing momentum diffusivity while thermal diffusivity remains relatively stable, leading to reduced Pr with increasing temperature. In this study, the aluminum plate's high thermal conductivity maintains Pr≈2.5~3 in the downstream region (y/d<10) due to elevated fluid temperatures.

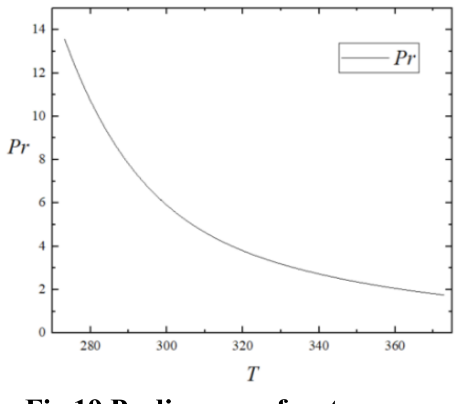

Fig.19 Pr diagram of water

For the heat transfer process following jet impingement on a wall surface, the fluid's thermal behavior can be approximated as boundary layer flow over a flat plate. Regarding heat transfer in boundary layer flows, given that 0.6≤Pr≤60, when the characteristic length in Re is taken as the plate length, the Nusselt number (Nu) at the wall surface is expressed as follows[30]:

$$\mathrm{Nu} = 0.0296\mathrm{Re}^{4/5}\mathrm{Pr}^{1/3} \tag{11}$$

Fig.20 illustrates the distribution of the Nusselt number (Nu) on the wall surface under varying jet inclination angles. At the stagnation point, Nu reaches its minimum value for all inclination angles considered. When the wall Nu is non-dimensionalized with wall distance, the momentum variation of the wall-adjacent fluid is found to be concentrated primarily near the impingement point. This region exhibits intense turbulence generation, enhancing the shear flow effect along the wall and consequently intensifying local heat transfer. Following impingement, the bulk fluid accelerates downstream along the wall. The momentum transfer from the jet toward the downstream direction produces a peak Nu value in this region. Conversely, in the upstream region, diminished fluid momentum results in lower flow velocities, leading to relatively poorer heat transfer performance and lower Nu values. Notably, a secondary (smaller-magnitude) Nu peak emerges near the impingement point in the upstream region. As the fluid continues to diffuse, convective heat transfer diminishes due to progressive velocity decay along the wall. Consequently, regions of higher Nu remain confined primarily to the downstream region.

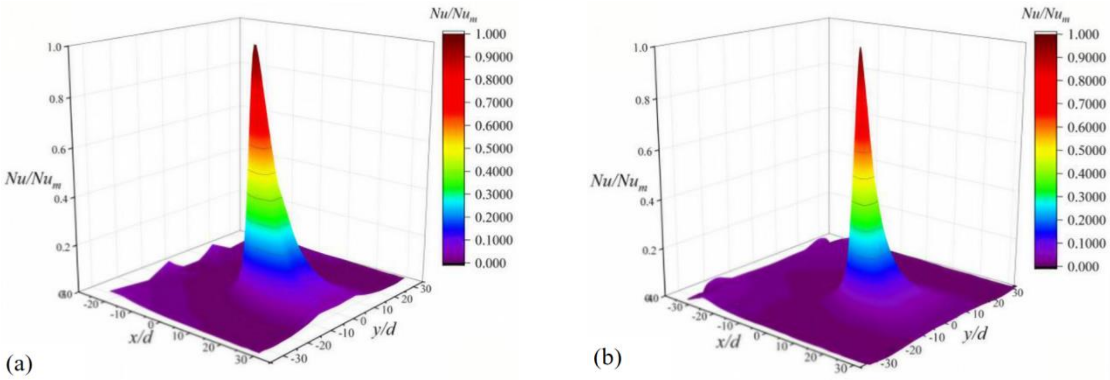

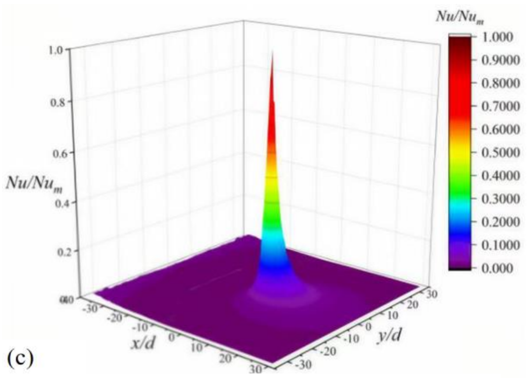

Fig. 20 Nu diagram of the wall for different jet inclinations; (a)θ=60°, (b)θ=45°, (c)θ=30°

For the 60° inclination case, the increased jet inclination shifts the Nu peak location further downstream along the wall. Within the oval-shaped region defined by $1.18 < x/d < 7.56$ and $y/d < 2.06$, the ratio Nu/Nu_m exceeds 0.6, indicating an area of enhanced heat transfer performance. This high-efficiency zone exhibits greater spatial coverage compared to the 30° and 45° inclination cases. Radial decay of Nu occurs rapidly when moving outward from the center along both x/d and y/d directions. In the downstream wall region beyond x/d>15.6 and y/d>4.8, Nu/Num values fall below 0.2. As the distance from the stagnation point increases further, Nu/Num approaches zero. Within this region, diminished fluid velocities result in significantly degraded heat transfer efficiency.

For inclination angles of 30° and 45°, the downstream wall region exhibits a comparatively smaller zone of elevated Nu values. At θ = 30°, the Nu/Nu_m ratio declines to 0.6 at coordinates (x/d = 2.67, y/d = 0) and (x/d = 0.01, y/d = 1.15). The corresponding elliptical domain spans 0.87 <x/d< 5.36 with y/d<1.89. With increasing distance from the stagnation point, Nu/Nu_m further drops to approximately 0.2 at (x/d = 5.5, y/d = 0) for the 30° case. For the 45° inclination, the elliptical region is bounded by coordinates (x/d = 7.03, y/d = 4.92) and (x/d = 10.83, y/d = 2.25).

5. Conclusions

This study established a multiphase flow numerical model for long-range inclined jet impingement on a wall based on a scaled nozzle configuration. By comparing three typical injection angles (30°, 45°, and 60°), the aerial dissipation characteristics of the jet and the evolution of the thermal-flow field on the impingement wall were systematically analyzed. The validity of the model was verified with experimental data.

Nevertheless, certain limitations remain in this study. During experiments, a slight delay in the thermal imaging camera caused a misalignment between the captured time points and the fixed simulation time steps. Additionally, pixel limitations of the thermal camera introduced some measurement errors in temperature readings, particularly in distal regions of the impact zone in upstream region. For the heat transfer process on the wall, which is dominated by fluid turbulence, the coupled turbulent k-ω model and multiphase flow solution accurately captured regions of high turbulence and heat exchange. Although some discrepancies exist in areas far from the stagnation point, this method still reliably predicts overall fluid temperature trends without affecting the main conclusions.

1. Jet inclination angle decisively influences wall-flow characteristics. During the deicing process with jets at different inclination angles, convection occurs between the jet and the ambient air, leading to continuous energy loss in the fluid and resulting in varying wall flow characteristics. When the jet inclination angle is 60°, the velocity loss is approximately 9.7%. As the inclination angle decreases, the extent of loss gradually reduces. At inclination angles of 45° and 30°, the losses are approximately 7.5% and 5.2%, respectively. Results show that at 30°, the spatial extent of the high-turbulence region is the largest, with a spanwise diffusion distance reaching ±16.15 d, approximately 36.5% greater than that at 60°. Meanwhile, at 60°, the flow Reynolds number significantly decreases in the upstream far region, approaching laminar state, whereas the 30° case maintains fully developed turbulence across the entire wall region, achieving a maximum Reynolds number of 2.91×10^5.

2. Local heat transfer efficiency is markedly modulated by the inclination angle. The Nusselt number (Nu) distribution reveals that at 30°, the high heat transfer zone ($Nu/Nu_m > 0.6$) covers the broadest spatial range (defined as $1.18 < x/d < 7.56$, $y/d < 2.06$), demonstrating optimal thermal uniformity. In contrast, the 60° case exhibits a narrow and concentrated high-efficiency zone, with Nu rapidly decaying to near zero in the upstream region. Compared to 60°, the 30° case increases the spanwise diffusion distance by approximately 36 d, shifting the thermal core region upstream from $x/d = -2.5$ (60° case) to $x/d = -13.5$ (30° case).

3. Comprehensive performance comparison identifies 30° as the optimal angle. Validation against experimental data confirms that the 30° inclination delivers the best overall heat transfer performance. This condition not only exhibits the strongest thermal diffusion capability—with a spanwise coverage of the high-temperature core region (>346.9 K) reaching ±25.8 d, far exceeding the ±7.8 d at 60°—but also extends the upstream thermal influence to $x/d = -13.5$ (compared to only $x/d = -2.5$ at 60°). Additionally, the 30° jet retains 92.5% of its exit velocity (higher than 90.3% at 60%), minimizing pre-impact momentum loss, and sustains a wall-jet velocity above 4.06 m/s. In summary, the 30° inclination performs optimally across multiple key metrics, including turbulence diffusion range (±16.15 d), and effective heat transfer area. Moreover, the jet at a 30° inclination angle also exhibits stronger impact pressure.

In conclusion, this study confirms that a 30° injection angle achieves the best balance among impact force, thermal diffusion capacity, and turbulence intensity, thereby providing a theoretical basis and design reference for optimizing spray gun angles in aircraft engine idle-state deicing operations.

Acknowledgment

The author acknowledge the financial supports from the Fundamental Research Funds for the Central Universities (No.3122023043).

Nomenclature

Symbols	T Temperature, [K]
d Nozzle diameter, [mm]	$\mathbf{u}$ Velocity vector, [m/s]
h Convective heat transfer coefficient, [W/(m²·K)]	u velocity, [m/s]
Nu Nu number	x Length in the x-direction, [mm]
Re Reynolds number	y Length in the y-direction, [mm]
Ri Richardson number	z Nozzle height, [m]
Pr Prandtl number	**Greek symbols**
Pe Péclet number	θ Jet inclination angles, [°]
k Thermal conductivity of the fluid, [$Wm^{-1}K^{-1}$]	α Thermal diffusivity, [m^2/s]
p Wall-Jet pressure, [Pa]	

Reference

[1] He, Q., Li, K., Xu, Z., Wang, J., Wang, X., Li, A., Research Progress on Construction Strategy and Technical Evaluation of Aircraft Icing Accretion Protection System, *Chinese Jiurnal of Aeronautics*, *36* (2023),10, pp.1-23.

[2] Li, B., *et al*., Dynamic Prediction for Aircraft Ground Deicing Operation Process, *Journal of Beijing University of Aeronautics and Astronautics*, *50* (2024), 1, pp. 224-233.

[3] Vertuccio, L., Foglia, F., Pantani, R., Guadagno, L., New Aircraft Anti/de-Icing Technologies, *IOP Conference Series Materies Science and Engineering*, *1024* (2021), 1, pp. 012012.

[4] Jiao, Y., Smart Operation System Enhances De-icing Support at Beijing Capital International Airport, *Air Transport and Business*, *407* (2019), 4, pp. 57-59.

[5] Xie, Y., Jiang, S., Research on Critical Performance Characteristics of Category E Aircraft Idle De-icing, *Scientific and Technological Innovation*, *33*, (2018), 2, pp. 43-44.

[6] Wang, Q., Peng, H., Wu, H., Zhang, Y., Su, Z., Study on Rheological Properties of Deicing / Anti-icing Fluids, *Applied Chemical Industry*, *45* (2016), 4, pp. 732-736.

[7] Jing, C., Y, Chang., Xing, Z., Yang, G., Study on the Dynamics of Slip and Detachment of Thin De-icing Fluid Films on Wing Surfaces, *Meccanica 59* (2024), 12, pp. 1-24.

[8] Chen, B., Wang, L. W., *et al*., Numerical Simulation and Experimental Validation of Aircraft Ground Deicing Model, *Advances in Mechnical Engineering*, *8* (2016), 5, pp. 1-15.

[9] Yakhya, S.,Morency, F., Numerical Study of Momentum and Heat Transfer in Propylene Glycol Jets Used for Aircraft Ground Deicing, Denver, Colorado. *23rd American Institute of Aeronautics and Astronautics Computational Fluid Dynamics Conference*, 2017.

[10]Ernez, S.,Morency, F., Eulerian, Lagrangian CFD Model for Prediction of Heat Transfer Between Aircraft Deicing Liquid Sprays and a Surface, *International Journal of Numerical Methods for Heat & Fluid Flow*, *29* (2019), 7, pp. 2450-2475.

[11]Ernez, S., Morency, F., CFD Model for Aircraft Ground Deicing:Verification and Validation of an Extended Enthalpy-porosity Technique in Particulate Two Phase Flows, *Fluids*, 2021,6:210.

[12]Ernez, S., Morency, F., A Multi-region CFD Model for Aircraft Ground Deicing by Dispersed Liquid Spray, *Energies*, *15* (2022), 7, pp. 6220.

[13]Yakhya, S., Ernez, S., Morency, F., Computational Fluid Dynamics Investigation of Transient Effects of Aircraft Ground Deicing Jets, *Journal of Thermophysics and Heat Transfer*, *33* (2019), 1, pp. 117-127.

[14]Pan, Y., Stevens, J., Webb, B, W., Effect of Nozzle Configuration on Transport in the Stagnation Zone of Axisymmetric,Impinging Free-surface Liquid Jets:Part 2—Local Heat Transfer, *Heat Transfer*, *114* (1992), 4, pp. 880–886.

[15]Zeraatkardevin, A., *et al*., A Three Dimensional Simulation of Spray Cooling and its Evaporating Liquid Film Generated on Patterned Surfaces, *International Journal of Multiphase Flow*, *115* (2022), 104174.

[16]Hajimohammadi, A., Zargarabadi, M. R ., Mohammadpour, J., A Detailed Analysis of Flow and Heat Transfer Characteristics under A Turbulent Intermittent Jet Impingement on A Concave Surface, *Thermal Science*, *26* (2022), 2c, pp.1709-1720.

[17]Ingole, S. B., Sundaram, K. K., Experimental average Nusselt number characteristics with inclined non-confined jet impingement of air for cooling application, *Experimental Thermal and Fluid Science*, 77 (2016), pp. 124-131.

[18]Baghel, K., *et al*., Free Surface Oblique Liquid Jet Impinging on a Flat Surface:Towards Improved Understanding of Flow Structures and Heat Transfer, *International Journal of Thermal Sciences*, 2023,194: 108552.

[19]Oliveira, A, V, S., Maréchal, D., *et al*., Experimental Study of the Heat Transfer of Single-jet Impingement Cooling onto a Large Heated Plate near Industrial Conditions, *International Journal of Heat and Mass Transfer*, *184* (2022), pp. 12814.

[20]Hosain, M. L., Fdhila, R. B., Daneryd, A., Heat Transfer by Liquid Jets Impinging on a Hot Flat Surface, *Applied energy*, *164* (2016), 8, pp. 934-943.

[21]Liu, C., Huang, Z., Tang, C., Heat Transfer Characteristics of Oblique Jet Impingement Liquid Film Cooling in the Forced Convection Mode, *International Journal of Heat and Mass Transfer*, 46 (2025), 10, pp. 1-11.

[22]Rachdi, Z., Haien, N., Eladeb, A., et al., CFD Analysis of Heat Transfer Enhancement in Impinging Jet Array by Varying Number of Jets and Spacing, *Scientific Reports*, *15* (2025), 1, pp. 3023-3023.

[23]Wang, P., Lv. J., Bai, M., et al., Numerical Investigation of the Flow and Heat Behaviours of an Impinging Jet, *International Journal of Computational Fluid Dynamics*, *28* (2014), 6-10, pp. 301-315.

[24]Yang, B., Chen, Q., Luo, Y., et al., Numerical Study on the Effect of Round Jet Core Region Decay on Impingement Heat Transfer and Flow Characteristics over a Concave Surface, *Journal of Engineering Thermophysics*, *43* (2022),11, pp. 3041-3048.

[25]Ye, C., Numerical Simulation Study of Turbulent Jet Impact Wall Heat Transfer. Anhui: University of Science and Technology of China, 2017.

[26]Li, W., Wu, X., Wang, L., et al. Phase Field Simulation Research with COMSOL, *Science and Technology Vision*, *194* (2017), 8, pp. 54.

[27]Tyliszczak, A., Kuban, L., Stempka, J., Numerical Analysis of Non-Excited and Excited Jets Issuing from Non-Circular Nozzles, *International Journal of Heat and Fluid Flow*, *94* (2022), pp. 108944.

[28]Godi., Abraham., Pattamatta., et al. Evaluation of Candidate Strategies for the Estimation of Local Heat Transfer Coefficient From Wall Jets, *Experimental Heat Transfer*, 2020, 33(1), pp. 40-63.

[29]Lee, H. G., Kim, J., Two-dimensional Kelvin-Helmholtz Instabilities of Multi-component Fluids, *European Journal of Mechanics-B: Fluids*, *49* (2015),8, pp.77-88.

[30]Incropera, Frank, P, et al., *Fundamentals of Heat and Mass Transfer*, John Wiley and Sons Inc., New York, USA, 1996, pp. 559-618.

Received: 25.07.2025.
Revised: 02.10.2025.
Accepted: 13.10.2025